Journal of Sailing Technology 2026, volume 11, issue 1, pp. 95 – 114.
The Society of Naval Architects and Marine Engineers.

Comparative Analysis of Wind Load Application Techniques for Aeroelastic Analysis of Hard Wingsails

Mekete Mulualem Mebratu
Ghent University, Belgium, mekete.mebratu@ugent.be.

Kris Hectors
Ghent University, Flanders Make @Miro, Belgium.

Wim De Waele
Ghent University, Flanders Make @Miro, Belgium.

Manuscript received October 14, 2025; revision received February 19, 2026; accepted March 8, 2026.

Abstract. Reliability analysis of mechanical systems requires precise evaluation of structural responses in critical components. In aeroelastic analysis, the fidelity of these responses depends on accurate modeling and transfer of aerodynamic loads between fluid solvers and structural solvers. Although several CFD-to-FE load transfer methods exist, comparative assessments for wingsail structures remain limited. This study investigates the aeroelastic response of hard wingsail components using three aerodynamic load transfer methods, assessing both structural response predictions and computational time. The first method uses a Lifting-line method, transferring aerodynamic loads directly to the lifting-line. The second is a panel-based method based on the 3D vortex lattice model, integrating CFD and structural mechanics via the DLOAD subroutine in Abaqus v2023. The third is similar but uses a field-mapping technique for load transfer. These methods are evaluated for single-element and two-element wingsails. Aerodynamic pressure coefficients for the single-element configuration are obtained using XFOIL 6.99; experimental data inform the two-element wingsail. Results indicate that the lifting-line method predicts higher von Mises stress in the root region of the main load-bearing steel component, but lower stresses in the core and face-sheet regions of the leading-edge sandwich composite. Structural stresses in the root regions of the leading edge and spar-box components of the wingsail obtained using the DLOAD subroutine strongly agree with the mapped field method. However, the DLOAD subroutine demonstrates superior computational speed, requiring approximately 30% less wall-clock time than the mapped field method at higher core counts, while maintaining nearly equivalent deformation predictions.

Keywords: Wingsail; lifting-line method; vortex lattice method; field mapping; DLOAD subroutine; finite element analysis; wind-assisted propulsion.

NOMENCLATURE

A_S Sail segment area [m²]
$B_k(\mathbf{x}_k)$ Radial basis function associated with data site $\mathbf{x}_k$[-]
C Total chord [m]
$\mathrm{C1}$ Main wing chord [m]
$C2$ Flap chord [m]
C_D Aerodynamic drag coefficient [-]
C_k Interpolation coefficient associated with the k^{th} basis function [-]
C_L Aerodynamic lift coefficient [-]
C_p Aerodynamic pressure coefficient [-]
$C_p(\bar{x}_i, \bar{y}_i)$ Pressure coefficient at the middle of a discretized panel [-]

Downloaded from http://onepetro.org/JST/article-pdf/11/01/95/5341453/sname-jst-2026-05.pdf/1 by guest on 26 March 2026

D Aerodynamic drag force [N]
ΔD Resultant displacement [mm]
d_k Euclidean distance between source point k and target point $\mathbf{x}$ [m]
H Reference height [m]
h Span length [m]
L Aerodynamic lift force [N]
M Aerodynamic moment [N m]
N Total number of data points [-]
p User-defined power parameter controlling distance weighting [-]
ΔP Aerodynamic surface gauge pressure [Pa]
$\Delta P(\mathbf{x})$ Interpolated pressure value at spatial location $\mathbf{x}$ [Pa]
$\Delta P(\mathbf{x}_k)$ Known k^{th} data (source) point pressure value [Pa]
$R(x_{ref}, y_{ref})$ Vortex point [m]
Re Reynolds number [-]
U Wind speed [m s^{-1}]
U_{10} Mean wind speed at a 10-meter reference height [m s^{-1}]
U_∞ Free-stream velocity [m s^{-1}]
V Local air velocity on a panel's surface [m s^{-1}]
w_k Distance-based interpolation weight for source point k [-]
$\mathbf{x}$ Spatial coordinate of the evaluation point (x, y, z) [m]
$\mathbf{x}_k$ Spatial coordinate of the k^{th} data (source) point [m]
Z Vertical position above sea level [m]

α Wind shear exponent [-]
β Flap wing deflection angle [°]
ε Shape parameter controlling the spread of the MQ basis function [-]
θ Main wing angle of attack [°]
ρ Air density [kg m^{-3}]
$\sigma_{p,\text{facesheet}}$ Principal stress in a sandwich panel face sheet [MPa]
σ_v Von Mises stress [MPa]
τ_{core} Shear stress in a sandwich panel core [MPa]

2D Two-Dimensional
3D Three-Dimensional
CAE Complete Abaqus Environment
CFD Computational Fluid Dynamics
CPU Central Processing Unit
FE Finite Element
FSI Fluid-Structure Interaction
MQ Multiquadric
TPS Thin Plate Spline
WAPS Wind Assisted Propulsion Systems

1. INTRODUCTION

Wind-assisted propulsion has re-emerged as a promising solution to reduce fuel consumption and emissions in the shipping industry. In January 2023, the European Union Horizon Europe funding program approved funding for the ORCELLE Wind project, which aims to develop and build a wind-powered roll-on/roll-off (ro-ro) cargo vessel. The ORCELLE project focuses on developing and demonstrating wind as the primary propulsion source for commercial shipping, achieving average energy efficiency gains of over 50% through the construction of physical demonstrators and the refinement of advanced simulation and routing tools (2023). The project employs wingsail technology mounted on ships to generate aerodynamic thrust for propulsion, as shown in Fig. 1.

Downloaded from http://onepetro.org/JST/article-pdf/11/01/95/5341453/sname-jst-2026-05.pdf/1 by guest on 26 March 2026

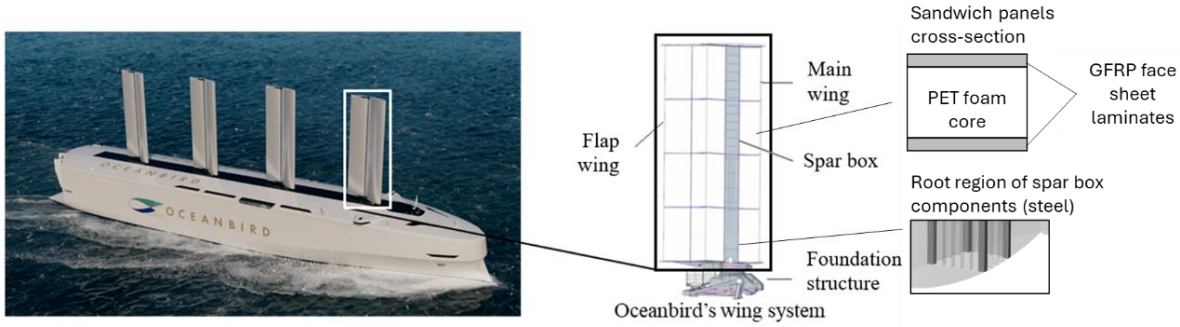

Figure 1. The world's first wind-powered Ro-Ro vessel (© Oceanbird).

The hard wingsail primarily consists of high-strength steel (S690QL) for the spar-box and foundation structure and composite sandwich panels for the sail. These composite sandwich panels are made up of a Polyethylene Terephthalate foam core and Glass Fibre Reinforced Polymer face sheet laminates. The structural integrity and fatigue performance of the wingsail are governed by the behaviour of critical components and mechanical joints within the system. Analysis of the wind-induced structural responses of the spar-box and its connection with the foundation structure (indicated in Fig. 1), is crucial, as it is the primary load-bearing subsystem.

Composite sandwich panels are susceptible to various failure modes under fatigue loading, including tension or compression failure of the facings, shear failure of the core, wrinkling failure of the compression facing, local indentation, debonding of the core/facing interface, and global buckling. The initiation, propagation, and interaction of these failure modes depend on the type of loading, the constituent material properties, and the geometrical dimensions (Sharma et al. 2006). Shear failure of the foam core dominates, especially when subjected to high shear forces during manoeuvres or strong wind conditions, as cyclic loading reduces the residual shear strength of the foam core, leading to face sheet fracture and face sheet/core delamination. Life prediction can be simplified by using the stress in the core (Ma et al., 2021). In low-load, high-cycle scenarios, tensile failure of the face sheets is also a significant design concern (Zenkert and Burman, 2011). Most fatigue damage models' rules form the basis for life analysis with methods considering either the dominant core shear failure mode or both main failure modes of face sheet tension/compression fracture and core shear failure (Ma et al., 2021; Suzuki and Mahfuz, 2018). A thorough understanding of these failure mechanisms is therefore essential for the reliable design and long-term operation of wind-assisted propulsion systems.

1.1. Fluid-Structure Interaction and Aeroelastic Analysis

The aeroelastic analysis of wingsails falls within the broader domain of fluid-structure interaction (FSI) problems, which involve the dynamic interplay between aerodynamic forces and structural responses. The coupling of computational fluid dynamics (CFD) with computational structural mechanics forms the foundation of FSI modeling, with one-way and two-way coupling strategies offering a balance between computational efficiency and predictive accuracy.

Two-way coupling, which involves mutual feedback between aerodynamic load and structural deformation, is ideal for cases with significant structural deflection (Schwab and Reid, 2020). However, its computational cost can be prohibitive for large-scale parametric studies (El et al., 2023; Schwab and Reid, 2020), and most of the coupled solvers use an implicit method (Xu and Peet, 2017). In the implicit method, the structural model and flow model exchange information at every inner iteration of the time step within the solver; it is computationally unstable and prone to divergence (Schwab and Reid, 2020; Xu and Peet, 2017). In the explicit methods, the fluid and structural domains are solved sequentially, with data exchanged only once per time step. One-way coupling, which is based on aerodynamic load applied to a structural model without accounting for structural feedback, is commonly employed in the aeroelastic analysis for wind turbine blades

Downloaded from http://onepetro.org/JST/article-pdf/11/01/95/5341453/sname-jst-2026-05.pdf/1 by guest on 26 March 2026

(Abdullah et al. 2022; Zhang et al., 2023; Huque et al., 2024). It is also often sufficient for early-stage design cases of moderate deformation scenarios, such as those encountered in wingsail applications. Its validity is supported by comparative studies showing minimal performance deviation from two-way coupling. For instance, accounting for rotor elasticity through a two-way coupling approach increases the predicted rotor power and thrust by approximately 1% and 0.3%, respectively, compared with a rigid-blade assumption (i.e., effectively one-way coupling) for the generic DTU 10 MW horizontal-axis wind turbine (Sayed et al., 2019). This study adopts a one-way coupling strategy, transferring aerodynamic loads to the structural finite element (FE) model. This suitability is further evidenced in recent studies on wind turbine blades with modified geometries, where computationally efficient one-way FSI analysis is explicitly used to investigate structural stress and deformation for design optimization (Huque et al., 2024).

Hard wingsails, like aircraft wings, experience complex and non-uniform aerodynamic surface pressure, the local pressure field generated by the surrounding airflow, across their surfaces. High-fidelity computational fluid dynamics (CFD) methods such as Reynolds-Averaged Navier-Stokes, Large Eddy Simulation, and Detached Eddy Simulation can solve complex viscous, separated, and vortex-dominated flows (Zhu, 2024). For the preliminary design and rapid parametric studies, two commonly used simplified aerodynamic load modeling methods are the lifting-line and vortex lattice methods (Cirello et al., 2025; Gulizzi and Benedetti, 2024; Sugar-Gabor, 2018). In the lifting-line method, the aerodynamic lift distribution over a wing is modelled by representing the wing as a bound vortex line, with spanwise variations in circulation used to compute the aerodynamic loads. In contrast, the vortex lattice method divides the lifting surface into a grid of panels, where the bound vorticity is represented by a lattice of vortex filaments.

One of the challenges in computational methods to fluid-solid interaction is facilitating data exchange between non-matching meshes, as the fluid and solid domains often require different mesh types and resolutions (Du et al. 2024). In the computational aeroelastic analysis, once aerodynamic loads are computed using CFD or simplified methods, they must be transferred from the aerodynamic mesh to the structural finite element (FE) model. The choice of CFD-to-FE load transfer method can influence the accuracy of the predicted structural responses and computational efficiency of design studies. Various load transfer methods have been developed, including radial basis function interpolation, conservative cell-integration schemes, and force/moment-conserving mapping techniques (Beom Lee et al. 2023; Chiappa et al. 2024, 2024; Du et al. 2024). Radial basis function interpolation is limited by high computational cost and sensitivity to geometric nonlinearity or simplified structural models, which can introduce load-transfer errors (Buhmann et al. 2020). A local projection method using dimensionality reduction and cell-surface integration reduces these errors and improves efficiency by minimizing the number of required source–target evaluations (Du et al. 2024). While comparative studies of load transfer methods exist in aerospace or turbomachinery blades applications (Du et al., 2024; Valášek and Sváček, 2021), such multi-method comparisons are absent for marine wingsail applications. Existing wingsail aeroelastic studies have employed coupled CFD-FE frameworks (Zhu et al., 2024), but they have not compared alternative load transfer algorithms or examined their effects on the predicted structural responses of wingsail components. Additionally, a comprehensive comparison that simultaneously evaluate predicted structural response characteristics and computational efficiency across multiple methods for wingsail components remain lacking.

The focus of this work is the transfer of aerodynamic load data from two-dimensional (chordwise) experimental or CFD results to a three-dimensional FE model. The study is based on two sets of pressure-coefficient data for single-element and two-element wingsails. The aeroelastic responses of the leading-edge and spar-box components of a wingsail are compared for three different CFD-to-FE aerodynamic load transfer methods: a Lifting-line method, a DLOAD subroutine, and mapped field methods. This work addresses two primary research objectives: (1) the simultaneous evaluation of predicted structural response characteristics and computational time required across these load transfer methods, and (2) an investigation into the effects of these methods on component-level structural responses critical to wingsail design, specifically the main load-bearing spar-box and

Downloaded from http://onepetro.org/JST/article-pdf/11/01/95/5341453/sname-jst-2026-05.pdf/1 by guest on 26 March 2026

leading-edge sandwich composite components. The methods are compared in terms of predicted structural deformations, stresses, and associated computational costs. Details of the load transfer methods and the FE-model parameters for the wingsail are provided in Section 2. Section 3 presents the FE results for the root regions of the spar-box component and the leading edge of the main wing component. Conclusions are drawn in Section 4.

2. NUMERICAL METHODS

2.1. Aerodynamic Load on Wingsail

Wind Assisted Propulsion Systems (WAPS) generate auxiliary thrust from wind to reduce a ship's main engine load, thereby cutting fuel consumption. Wings for WAPS operate under gradient wind conditions in the atmospheric boundary layer (Li et al. 2023). This wind gradient can be described in terms of mean wind speed ($U_{(10)}$) in m/s at a reference height (H) of 10 metres above sea level. For WAPS, the most acceptable wind shear expression is the power law in which the wind speed (U) in m/s at a vertical position (z) in metres on the surface of the wingsail is computed using an expression as shown in Eq. 1 (DNV, 2022). This wind speed gradient model was employed to generate the three-dimensional pressure field data from chordwise 2D aerodynamic characteristics (coefficient of pressure) data of the wingsail, Eq. 2. The aerodynamic performance the wingsail system is considered at its upright condition, the analysis neglects aerodynamic interference effects between the vessel hull and the wing-sail array (Kramer and Steen, 2022), as well as mutual interactions, although notable interactions are reported (Zhu, 2024). The analysis also does not account for stochastic variations in aerodynamic loading or environmental uncertainty. The three-dimensional tip-loss effects and the influence of wing-tip vortices were excluded, assuming quasi-two-dimensional flow characteristics across the span to simplify the translation of chordwise data into the three-dimensional pressure field.

$$U = U_{(10)} \left(\frac{z}{H}\right)^{\alpha} \tag{1}$$

The wind shear constant, $\alpha = 0.12$, is the wind profile constant for wind on the open sea with waves. Wind-induced load acting on the wingsail structure can be described as pressure over the sail surfaces, as follows,

$$\Delta P = \frac{U^2 \rho \, C_p}{2} \tag{2}$$

where ΔP is surface gauge pressure in Pa, C_{p} is the coefficient of pressure across the wingsail surfaces, and ρ is the density of air in kg/m³. C_{p} is obtained from a CFD analysis. The following section discusses the methods employed to model this aerodynamic load in the aeroelastic FE analysis of the wingsail.

2.2. Load Transfer Methods

Accurate transfer of aerodynamic load across non-matching fluid–structure meshes is a central challenge in aeroelastic analysis, particularly when CFD solvers employ fine surface grids while structural finite element (FE) models use comparatively coarse discretization. This mismatch necessitates interpolation schemes that ensure numerical robustness and preserve both forces and moments. Early interpolation methods for one- and two-dimensional load-transfer problems include thin-plate splines (TPS), multiquadric (MQ) biharmonic interpolation, and inverse isoparametric mapping (IIM) (Smith et al. 2000). low-dimensional approaches remain relevant when aerodynamic inputs originate from two-dimensional CFD results (Du et al. 2024)

Downloaded from http://onepetro.org/JST/article-pdf/11/01/95/5341453/sname-jst-2026-05.pdf/1 by guest on 26 March 2026

Thin Plate Splines (TPS) are global radial-basis interpolants derived from minimizing the bending energy of a thin elastic plate. They are well suited for scattered data and do not require mesh connectivity, making them attractive for aerodynamic load-transfer applications (Smith et al. 2000). For a set of scattered points $\{(\mathbf{x}_k, \Delta P_k)\}_{k=1}^{N}$ on a 2D parameterized surface $\mathbf{x} = (x, y)$, the TPS interpolant is expressed as:

$$\Delta P(\mathbf{x}) = P(\mathbf{x}) + \sum_{k=1}^{N} w_k \ \phi(\| \mathbf{x} - \mathbf{x}_k \|), \tag{3}$$

where $P(\mathbf{x}) = a_0 + a_1 x + a_2 y$ is a first-order polynomial ensuring affine invariance, and w_k are the interpolation weights. The TPS kernel is given by:

$$\phi(d_k) = {d_k}^2 \ln d_k \, , \phi(0) = 0. \tag{4}$$

The d_k is the distance from point k to the target point in any dimension (should be greater than zero). This formulation yields a smooth, globally supported interpolant that naturally handles irregular node distributions. In one dimension, TPS reduces to the classical natural cubic spline. TPS has been widely used in mesh coupling due to its robustness and smoothness across non-matching discretization.

Multiquadric (MQ) Interpolation represents the field as a linear combination of radially symmetric basis functions cantered at the data locations. For scattered points $\mathbf{x_k}$, the classical MQ basis function is $\phi(d_\mathrm{k}) = \sqrt{{d_\mathrm{k}}^2 + \varepsilon^2}$, where ε is a user-selected shape parameter controlling the flatness of the basis. The interpolant for the pressure field is:

$$\Delta P(\mathbf{x}) = \sum_{\mathrm{k}=1}^{\mathrm{N}} w_\mathrm{k} \ \sqrt{\| \mathbf{x} - \mathbf{x_k} \|^2 + \varepsilon^2}. \tag{5}$$

Large values of ε yield broad, smooth approximations, whereas small values lead to sharper and more localized behaviour. MQ interpolation is mesh-free, dimension-independent, and highly flexible, making it effective for fluid–structure interaction where data points may be irregularly distributed. Its ability to produce smooth, high-quality approximations from scattered pressure data has contributed to its widespread use in aeroelastic coupling applications.

Inverse Isoparametric Mapping (IIM) is a projection-based technique that maps aerodynamic pressures to structural meshes. Löhner (1995) introduced efficient projection procedures for unstructured meshes grounded in finite element isoparametric concepts: the same element shape functions are used to interpolate both element geometry and the transferred pressure field. For each aerodynamic source point, an inverse mapping is solved to identify the corresponding parent-element coordinates in the structural mesh. Despite requiring a brute-force search across potential target elements, Smith et al. (2000) showed that IIM outperforms TPS and MQ in computational speed and memory efficiency for two-dimensional interpolation problems.

A key limitation is that IIM requires all source points to lie strictly within element boundaries; this issue is addressed in Abaqus/CAE's or Complete Abaqus Environment mapped-field algorithm, which includes secondary correction stages for points near or outside element edges. Given the range of available approaches and their differing performance characteristics, (1) the mapped field point cloud data transfer method, a built-in within Abaqus/CAE, (2) DLOAD subroutine method that uses projection mapping and interpolation, and (3) a lifting-line method, a simplified way of mapping surface pressures on the lifting line has been studied in this paper. The following subsections detail the implementation of each method.

Downloaded from http://onepetro.org/JST/article-pdf/11/01/95/5341453/sname-jst-2026-05.pdf/1 by guest on 26 March 2026

2.2.1. Mapped Field Method

The mapped field method involves the transfer of point cloud data, also called source data points, such as CFD pressure field data, to a structural FE model by mapping field values onto the target nodes or surface centroids. Abaqus/CAE attempts to map all source data points and their associated field values onto points in the target model, deciding whether to use or discard each source point based on search tolerance distance values. The positive and negative normal tolerance values define how far away a source data point can lie from the exterior surface of the target model, measured along the positive and negative normal vectors of the underlying geometry of the target surface, respectively. Their definitions are illustrated in Fig. 2. Any source points within these distances are mapped and included in the analysis.

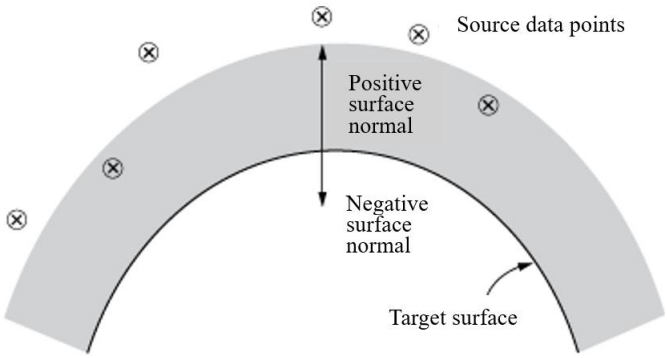

Figure 2. Point cloud mapping normal tolerances (Abaqus/CAE Users' Guide).

In this study, the maximum deviations between the XFOIL data points to the target surface are less than 0.5 mm and 1 mm towards the positive surface normal and negative surface normal, as shown in Fig. 3. In the case of XFOIL, the airfoil geometry was discretized into 160 points using the internal NACA coordinate generator within XFOIL. A positive normal tolerance of 1.5 mm and a negative normal tolerance of 4.5 mm are used to ensure that each source data point lies within the interpolation domain.

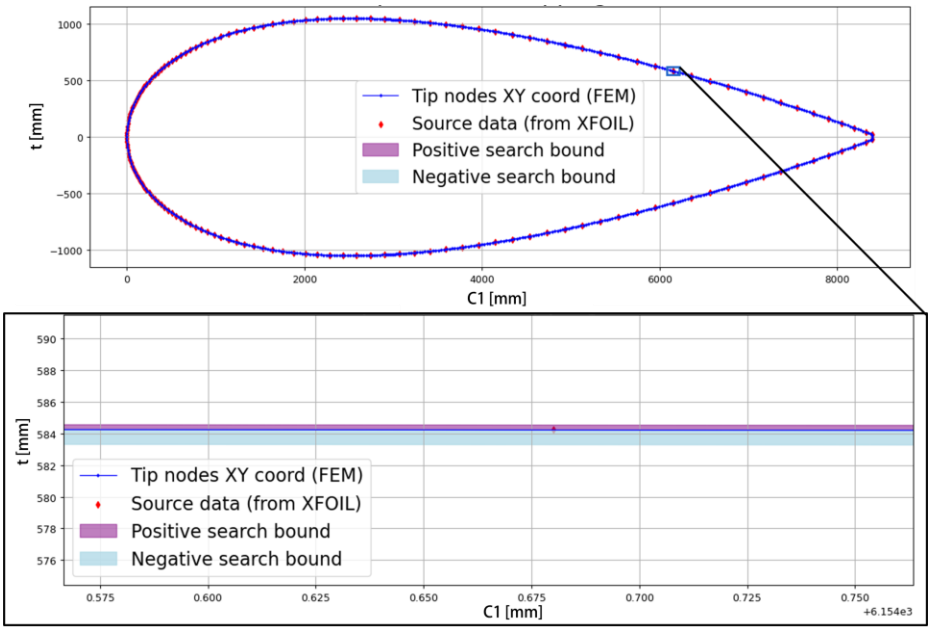

Figure 3. XFOIL point cloud data to meshed FEM surface mapping control.

Downloaded from http://onepetro.org/JST/article-pdf/11/01/95/5341453/sname-jst-2026-05.pdf/1 by guest on 26 March 2026

Abaqus/CAE makes three passes when attempting to map source points onto target points. First, it uses a distance weighting algorithm to interpolate the field data values on the meshed target model, always attempting to interpolate the source values on the target. The neighbourhood search tolerance is ignored on the first pass. If interpolation is not possible for any points, the second pass comes, the distance weighting algorithm takes nodes within the neighbourhood search distance, which is assumed in this study to be equal to the mesh size (30 mm). No sensitivity analyses were performed regarding the normal tolerances, the interpolation scheme, or the variation in the number of data points. The secondary step resembles local radial basis function interpolation and therefore may lead to misassignment of field values for very intricated surfaces, especially in curved regions with small radius of curvature. The distance weighting (w_{k}) can be expressed using Eq. 6.

$$w_{\mathrm{k}} = \frac{1}{d_{\mathrm{k}}^{p}} \tag{6}$$

The power term p is a user-defined parameter, and when a higher p is assigned, a stronger preference for close points will be taken, and w_{k} is the weight of point k. The normalized prediction or interpolation value of the field quantity(surface pressure $\Delta P(\mathbf{x})$) can be expressed using Eq. 7.

$$\Delta P(\mathbf{x}) = \frac{\sum_{\mathrm{k}=1}^{\mathrm{N}} w_{\mathrm{k}}\, \Delta P(\mathbf{x_k})}{\sum_{\mathrm{k}=1}^{\mathrm{N}} w_{\mathrm{k}}} \tag{7}$$

where $\Delta P(\mathbf{x_k})$ is the known k^{th} data (source) point pressure value. At the third pass of Abaqus/CAE, for any target points that remain unmapped, it applies the Default unmapped field value.

2.2.2. DLOAD Subroutine Method

The DLOAD subroutine in Abaqus/Standard allows to define non-uniform, time, and position-dependent mechanical loads. It can be used to apply pressure distributions obtained from CFD analyses onto surfaces of FE models, as demonstrated by Boudounit et al. (2020) in their wind turbine study. This is especially useful for complex geometries. In the current study, the spatial wind loads applied to the wing's FE model capture two distinct effects. Chordwise pressure data is derived from XFOIL and literature, while spanwise wind speed variations are represented by a power law wind shear profile. This load depends on element positions rather than deformations, making it effective for modeling diverse aerodynamic profiles.

In the DLOAD subroutine, the source data from any fluid solver must be transferred to the finite elements of the solid solver. The use of radial basis function (RBF) methods is one of the most common approaches for this purpose. However, the main limitations of radial basis functions include errors in simplified structural models (such as beams or shells), spatial non-linearity, and the significant computational effort required to solve the matrix equations (Du et al. 2024). In radial basis function interpolation, the method assigns weights based on the distance from target points to source points. The pressure differences between the suction and pressure sides of wingsails can lead to interpolation errors, particularly near the leading and trailing edges. It is observed in Fig. 4.

Figure 4 illustrates the implementation of “linear interpolation” used in the DLOAD subroutine method of the present study and its comparison with multiquadric (MQ), and thin-plate spline (TPS) RBF-based two-dimensional interpolation techniques. The pressure-coefficient data obtained from XFOIL simulations of a NACA0025 airfoil (under the conditions described in Section 2.4) was used to be transferred onto the finite-element integration points (target points). The accuracy of each interpolation was assessed using the root-mean-square error. All three methods successfully transfer the data, as confirmed by an RMSE value of zero. In MQ interpolation, the shape parameter ε controls the kernel behaviour. As ε decreases and approaches zero, the MQ interpolant converges toward linear interpolation. This characteristic is particularly important in highly curved regions, such as near the trailing edge, where pressure values on the pressure surface should not unduly influence

Downloaded from http://onepetro.org/JST/article-pdf/11/01/95/5341453/sname-jst-2026-05.pdf/1 by guest on 26 March 2026

those on the suction surface. Reducing ε minimizes this undesirable cross-surface interaction. This issue does not arise in the linear interpolation approach, as it relies solely on the two neighbouring source points that bracket the target point. Moreover, both source and target points lie on the same surface (either pressure or suction). The linear interpolation-based mapping improves computational efficiency relative to RBF methods by reducing local dimensionality and minimizing the number of weighting coefficients required between source and target points.

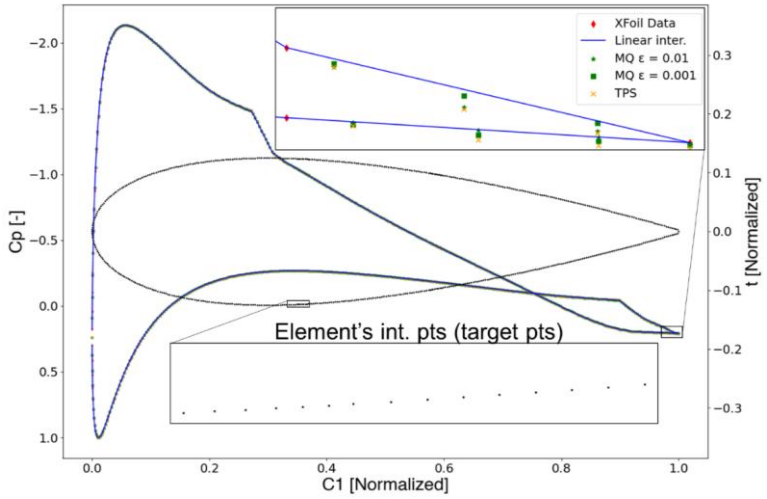

Figure 4. Implementation of two-dimensional interpolation of XFOIL pressure-coefficient data for a NACA0025 airfoil.

The DLOAD subroutine implemented in this study is analogous to a one-dimensional IIM procedure using the shape function of a two-node bar element: the pressure at an integration point between two source points is determined by, first mapping the source pressures to points along the curvature of the target model and then determining the pressure at the integration location through linear interpolation, as illustrated in Fig. 5. Since this study used two-dimensional (2D) chordwise pressure-coefficient data, chordwise interpolation was applied.

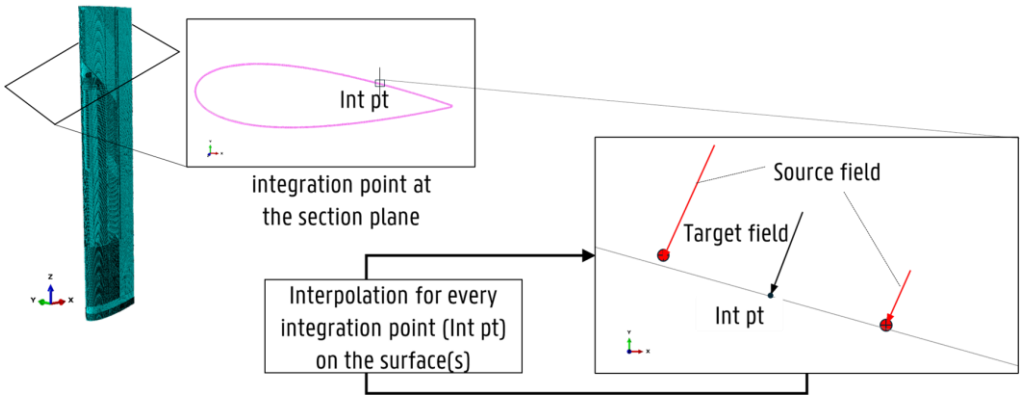

Figure 5. DLOAD subroutine-based aerodynamic load transfer method.

In this study, a Fortran script was developed to map pressure field data on the nodes of the surface of the FE model. At each integration point, the subroutine interpolates pressure coefficients from CFD data, multiplies by dynamic pressure to obtain local surface pressure, and applies this load to the structural mesh at the integration points of elements, shown in Fig. 5. A pseudo-code description of the DLOAD subroutine developed in this work for the single wingsail case is explained as follows. The same procedure applies to the two-element wingsail.

Downloaded from http://onepetro.org/JST/article-pdf/11/01/95/5341453/sname-jst-2026-05.pdf/1 by guest on 26 March 2026

```
FUNCTION
SUBROUTINE DLOAD(F,KSTEP,KINC,TIME,NOEL,NPT,LAYER,KSPT,COORDS,JLTYP,SNAME)
    // 1. EXTRACT ELEMENT POSITION AND DEFINE INPUT PARAMETERS
    GET X, Y, Z FROM COORDS
    // 2. COMPUTE DYNAMIC PRESSURE (Q)
    APPLY WIND SHEAR CORRECTION BASED ON HEIGHT (Z)
    CALCULATE APPARENT WIND VELOCITY AND THEN DYNAMIC PRESSURE (Q)
    // 3. COMPUTE AND APPLY ELEMENTAL SURFACE PRESSURE (F)
    IF (LOAD TYPE = SURFACE PRESSURE) AND (SURFACE = "MAIN WING") THEN
        IF PRESSURE SIDE (Y ≥ 0) THEN
            FIND Cp (LINEAR INTERPOLATE FROM PRESSURE COEFFICIENT TABLE)
            F = Cp × Q
        ELSE IF SUCTION SIDE (Y ≤ 0) THEN
            LINEAR INTERPOLATE FROM PRESSURE COEFFICIENT TABLE
            F = Cp × Q
        END IF
    END IF
END FUNCTION
```

2.2.3. Lifting-Line Method

Lifting-line method aligns with the methodology applied in the work of Deng et al. (2024), where (1) the blade is converted into a linear beam model with a small number of structural elements, and (2) the CFD resolved surface pressure and viscous stresses are integrated into normal forces and directly applied to the corresponding structural nodes. This process is consistent with established lifting line principles because the lifting line fundamentally represents a blade through its spanwise circulation (or equivalently, sectional normal force), rather than through full geometric resolution. The lifting line theory is a classical aerodynamic analysis technique used to predict the lift distribution and induced drag of finite wings. The lifting line theory represents the wing as a single spanwise line of bound circulation, positioned at the quarter-chord, and neglects chordwise load distributions. The detailed surface pressure distribution results are simplified using the lifting-line method. The wing is modelled as a bound vortex line with spanwise-varying circulation, allowing the complex three-dimensional pressure field to be approximated in terms of equivalent lift, induced drag, and moment along the vortex line. The application of the discrete lifting-line method for the representation of aerodynamic load on WAPS single-element sails has been validated by Kramer and Steen (2022). The method is also employed in different studies, such as aircraft wing-box design optimization (Boudounit et al., 2020), wind turbine fatigue calculation (Fritz et al. 2022), and aeroelastic optimization of aircraft wings. The vortex line is discretized into segments, with the resolution of the discretization adapted from the findings of Kramer and Steen (2022). They showed that for a wingsail with 56 meters of span length, the lift and drag with 10 vortices at an angle of attack of $10°$ only differed from a test with 100 vortices by roughly 4%. The current study discretizes 40 meters of span length of the wingsail into 20 segments. Control points are defined at the midpoints of the bound vortices, where the induced velocities are evaluated. These control points are treated as the points of load application. The imaginary line connecting all such points is hereafter referred to as the load reference axis.

Since the wing in this study is without sweep and tip effect consideration, the locus of aerodynamic centres is assumed to be a straight line. Hence, the bound vortex filament is assumed not to affect the effective angle of attack (Reid and Hunsaker, 2021). While these assumptions are derived for high-aspect-ratio aircraft wings, they are particularly valid for wingsails since wingsails operate significantly at lower operational speeds and they have substantially higher aspect ratios compared to typical aircraft wings. The vortex strength along the span is assumed to be constant; therefore, uniform aerodynamic coefficient values are used across the span of the wingsail. The details of the lift and drag calculations are discussed in Section 2.4.

Downloaded from http://onepetro.org/JST/article-pdf/11/01/95/5341453/sname-jst-2026-05.pdf/1 by guest on 26 March 2026

2.3. FE Model Parameters

The detailed geometrical features, including the boundary conditions of the wingsail for the FE model, are taken from the early-stage Oceanbird's two-element wingsail design parameters, as shown in Fig. 6. The main and flap wing airfoil types are NACA0025 and NACA0015, respectively. The wingsail has a total chord length (C) of 14 meters, with the main wing chord $(C1)$ measuring 8.4 meters. The span length (h) is 40 meters. The main load-bearing components of the wingsail are the four two-stage stepped, at the middle of its height, hollow section spar components within the spar-box. The thickness of these spars is 25 mm. The skin of the wingsail is made from sandwich panels. The face sheet thickness of 3.5 mm and a core region thickness of 40mm have been taken.

The aerodynamic loads are modelled for the largest true wind speed of 10m/s and vessel speed of 10m/s at head wind that gives an apparent wind speed of 20m/s which are based on the Oceanbird's preliminary design values and air density of 1.35 kg/m³.

Material properties include a Young's modulus of 210 GPa and a Poisson's ratio of 0.3 for steel. The shear modulus of the sandwich core region and the Young's modulus of the face sheet of the sandwich panel are 28.5 MPa and 15 GPa, respectively (Xie et al., 2022).

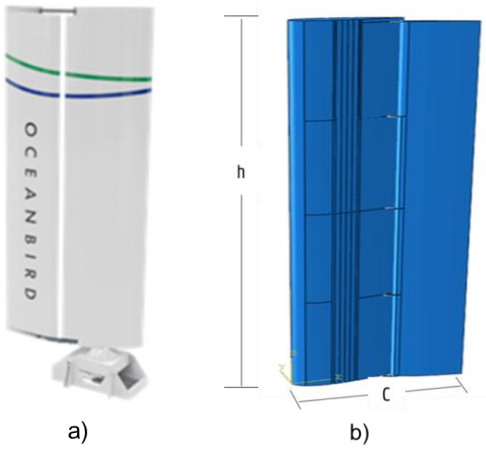

Figure 6. a) Design model of Oceanbird's two-element wingsail and b) simplified Abaqus model.

The aeroelastic structural analysis was conducted using Abaqus v2023. Quadrilateral shell elements and quadratic beam elements are used for the finite element discretization. A mesh sensitivity analysis was performed, and mesh convergence was achieved with an element size of 30mm, verified using the extrapolated von Mises stress at the root section of the spar-box component. For the two-element wingsail configuration, the mesh comprised 1,087,661 total elements (1,082,537 linear quadrilateral elements of type S4R, 71 linear triangular elements of type S3, and 5,053 linear line elements of type B31). The single-element wingsail configuration consisted of 1,028,247 nodes and 1,035,417 total elements (1,030,364 linear quadrilateral elements of type S4R and 5,053 linear line elements of type B31). All FE analyses were conducted on a workstation with 256GB of RAM and Intel(R) Xeon (R) Gold 6152CPU @ 2.10 GHz. Computational cost analysis was conducted across varying levels of parallelism, utilizing 2, 4, 8, 12, and 16 parallel cores.

2.4. Single-Element Wingsail

XFOIL 6.99 (Drela, 1989) software was used to generate the coefficient of pressure distribution across the single-element wingsail airfoil. While XFOIL is typically most accurate for thinner airfoils (thickness/chord < 15%) at moderate Reynolds numbers $(Re < ½ \text{ million})$, validation studies have demonstrated acceptable performance for thicker profiles in the subcritical Reynolds number regime. Von Klemperer et al. (2023) validated XFOIL predictions for the 20% thick NACA0020 airfoil across $Re = 1.5 \times 10^5$ to 1.0×10^6 through wind tunnel experiments and CFD comparisons, demonstrating

Downloaded from http://onepetro.org/JST/article-pdf/11/01/95/5341453/sname-jst-2026-05.pdf/1 by guest on 26 March 2026

good agreement for lift coefficients in the linear regime. Similarly, Ko (2022) stated that XFOIL showed good agreement with experimental data for lift coefficients, especially in the linear region for thick airfoils. The primary limitations concern prediction accuracy near stall and with significant flow separation; however, we assumed that for eight-degree angles of attack where flow remains predominantly attached, XFOIL provides reliable pressure distribution predictions suitable for aeroelastic load transfer analysis for the NACA0025 airfoil at $Re = 5 \times 10^5$. Therefore, XFOIL's viscous-inviscid coupling method asumed remains valid for the current study.

XFOIL uses a low-order panel method to solve the airfoil flow. It is based on inviscid, incompressible potential flow theory, coupled with boundary layer and wake models to account for viscous effects. XFOIL discretizes the airfoil into panels that allow for the approximation of the flow field around the airfoil. It uses Bernoulli's principle to compute the pressure coefficient at the middle of a panel, $C_{\mathrm{p}}(\bar{x}_i, \bar{y}_i)$, according to Eq. 8.

$$C_{\mathrm{p}}(\bar{x}, \bar{y}) = 1 - \frac{V^2}{{U_\infty}^2} \tag{8}$$

where V is the local velocity on the surface of the discretized panel and U_∞ is a free-stream velocity (Drela, 1989). For the present analysis, the airfoil was discretized into 160 panels, and the flow was analysed at a Reynolds number of 5×10^5, corresponding to a wind speed of 20 m/s (Li, Wang and Sun, 2020), and the Mach number was maintained below 0.005 to ensure incompressible flow conditions. To represent average wind tunnel conditions, we used an $\mathrm{N_{crit}}$ (or N-factor) of 9. This parameter defines the transition from laminar to turbulent boundary layers (Drela, 1989). The solution was run for ten iterations to ensure convergence, after which the pressure coefficient was extracted at the centre of each panel. Figure 7a illustrates how the chordwise pressure coefficient of a single-element wingsail with a chord length $(\mathrm{C1})$ varies across the surface at an angle of attack equal to 8 degrees. This figure shows a significant inversion of pressure between the leading and trailing edges on both sides of the wingsail. At the pressure side, the pressure becomes markedly negative at a short distance from the leading edge, indicating the onset of the local flow separation and then transition to turbulent flow before re-attaching, which then re-attaches near the trailing edge of the airfoil. This pressure coefficient data is directly utilized for the DLOAD subroutine and mapped field methods.

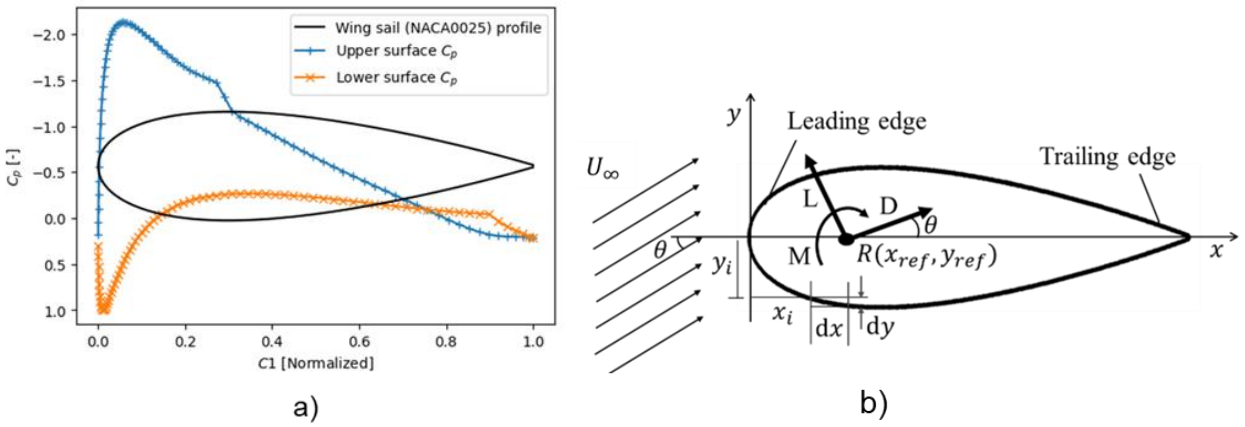

Figure 7. a) Coefficient of pressure across the surfaces of the NACA0025 airfoil at an 8° angle of attack and Reynolds number of 5×10^5, and b) equivalent lift, drag, and moment loads at the reference point (25% of wing chord length).

For the lifting-line method, the coefficient of pressure data obtained from XFOIL is represented by equivalent lift, drag, and moment coefficients at a reference point or vortex point, $R(x_{ref}, y_{ref})$, Fig. 7b. The lift and drag forces on each segment of the wingsail are defined as the force components

Downloaded from http://onepetro.org/JST/article-pdf/11/01/95/5341453/sname-jst-2026-05.pdf/1 by guest on 26 March 2026

acting normal and parallel, respectively, to both the incoming velocity and the vortex line that passes through the vortex point $R(x_{ref}, y_{ref})$ throughout the span length of the wingsail. The lift, drag, and moment coefficients are calculated from the coefficient of pressure data for each panel of the airfoil, c_p, obtained from XFOIL shown in Fig. 7a, using Eqs. 9-12.

$$C_L = c_y \cos\theta - c_x \sin\theta \,;\ \text{and}\ C_D = c_y \sin\theta + c_x \cos\theta \tag{9}$$

$$c_x = \oint c_p dx;\ and\ c_y = \oint c_p dy \tag{10}$$

$$C_M = \oint -c_p\big((x - x_{ref})dx + (y - y_{ref})dy\big) \tag{11}$$

The lift force L, drag force D, and moment M, at each reference point can be expressed as:

$$C_L = \frac{L}{0.5\rho U^2 A_S};\ C_D = \frac{D}{0.5\rho\, U^2 A_S};\ C_M = \frac{M}{0.5\rho U^2 A_S L_{cs}} \tag{12}$$

where A_S is the segment area or the total sail area divided by the number of segments, C_D is the drag force coefficient, C_L is the lift force coefficient, and L_{cs} is the chord length of a single element wingsail.

2.5. Two-Element Wingsail

For the two-element wingsail aeroelastic analysis, the aerodynamic load is based on Oceanbird's two-element wingsail design. The experimental pressure field data based on the aerodynamically favourable configuration of the main and flap wings is assumed. The optimal angle of attack for wingsails is very close to stall (Vinje Kramer and Steen, 2022). Precise knowledge of the aerodynamics near stall, including hysteresis effects, forms the basis of any automated trimming strategy for a wingsail-assisted propulsion system (Hillenbrand et al., 2024). Operating close to stall is assumed to be favourable, as it enables the obtaining of the maximum lift coefficient. Hillenbrand et al. (2024) conducted a series of wind tunnel tests to investigate the stall behaviour of a two-element wingsail having NACA0025 and NACA0015 profiles for the main and flap wings, respectively, to assess its implications for automated trimming. At a flap wing deflection angle of 15° relative to the main wing, their study identified two stall conditions.

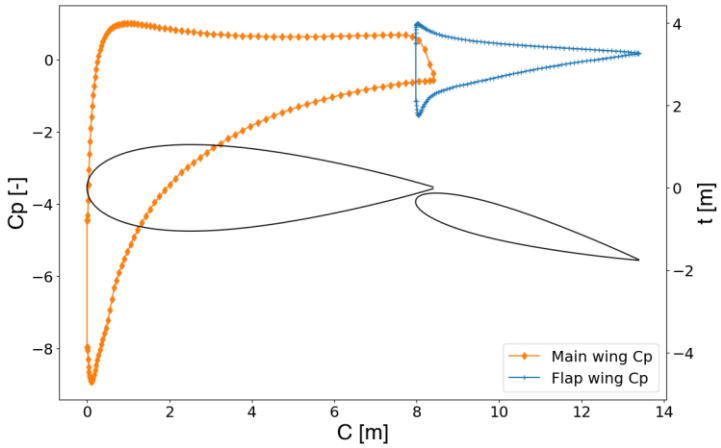

Figure 8. Coefficients of pressure distribution across the chord length of two-element wingsail at the main wing angle of attack of 22° and flap deflection angle of 15° relative to the main wing.

Downloaded from http://onepetro.org/JST/article-pdf/11/01/95/5341453/sname-jst-2026-05.pdf/1 by guest on 26 March 2026

From the perspective of a trimming strategy aimed at maximizing aerodynamic lift, the optimal main wing angle of attack would therefore be close to the first stall condition (Hillenbrand *et al.*, 2024). However, deviations from this optimal state are expected due to the fluctuating nature of the wind and ship motions. An automated control system must respond to these variations and adapt the wingsail trim accordingly. Their findings also showed that avoiding the second stall stage can result in significant benefits in two ways: the loss of aerodynamic force is reduced, and the required decrease in main wing angle of attack or actuation range needed for force recovery through flow reattachment is smaller. In this study, a wingsail configuration with a main wing angle of attack of 22°, just before the onset of the second stall condition (Hillenbrand et al., 2024), and a flap wing deflection angle of 15° is adopted as the reference case for obtaining the pressure coefficient used as the wind load input. Test data for the pressure coefficient distribution of a model-scale version of Oceanbird's wingsail under these conditions were provided and are shown in Fig. 8. Their study outcomes are valid for the tested scale with a Reynolds number of 0.73×10^6. It has also been stated that the transfer of these outcomes to two-element wings and wingsails of other planforms and geometries, especially considering the gap dimensions, and flow characteristics in terms of Reynolds number and turbulence intensity, is complex and must be considered carefully. The current study has directly adopted their coefficient of pressure data, and the surface pressure field data is computed using Eq. 2, and transferred into the FE model using mapped field and DLOAD subroutine method.

3. RESULTS AND DISCUSSION

Some illustrative aeroelastic responses of the main load-bearing component of the spar-box, face sheet, and core regions of the leading edge composite sandwich component of the wingsails are discussed. Fig. 9 shows the von Mises stress (σ_v) in the root region of the heavily loaded spar-box component, obtained using three distinct load transfer methods. The lifting-line method appears to yield relatively larger stresses as compared to the other methods. This indicates that representing the distributed aerodynamic load as equivalent lift, drag, and moment loads along a lifting line results in relatively higher stresses in the main load-bearing spar-box component.

Fig. 10b and 10c show the shear stress in the sandwich panel core region (τ_{core}) and the maximum principal stress in the face sheet ($\sigma_{\text{p,facesheet}}$) of the "Leading-edge" component near the bottom of the wingsail ($0 < z < 200$ mm), respectively. At the nose of the leading edge, both the shear and principal stresses predicted by the lifting-line method are notably lower than those obtained from alternative methods. This is due to the method's inherent limitation in fully representing the spatial distribution of local aerodynamic loads. The local wind loads distributed on the leading edge surface are transformed into concentrated loads applied on the load reference axis. Although the total aerodynamic load exerted on the wingsail has been transferred, the transformation of a distributed load into a relatively concentrated form alters local aeroelastic responses in some regions. In contrast, the DLOAD subroutine and mapped field loading methods capture local load effects more realistically, with results that are closely aligned.

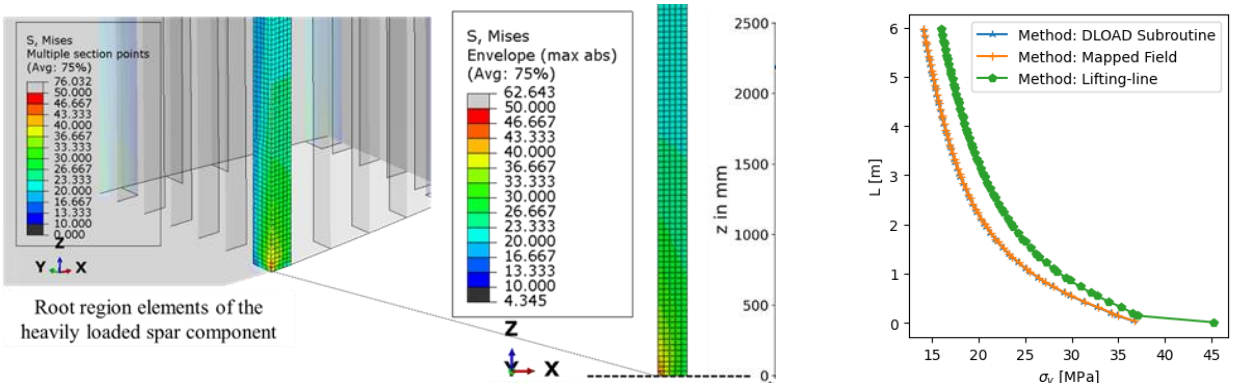

Figure 9. Von Mises stress of the root section of the heavily loaded spar component.

Downloaded from http://onepetro.org/JST/article-pdf/11/01/95/5341453/sname-jst-2026-05.pdf/1 by guest on 26 March 2026

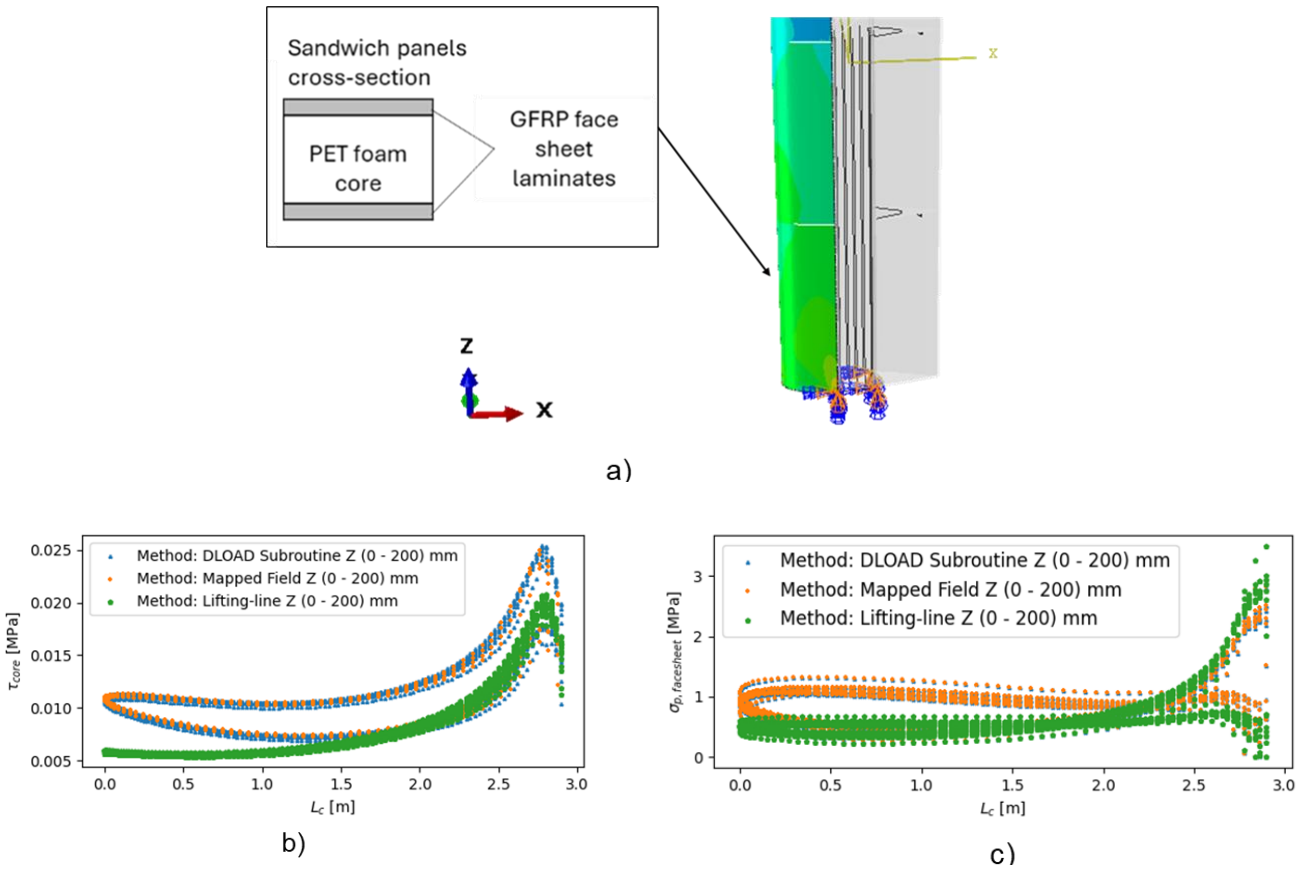

Figure 10. a) Leading-edge component of the wingsail, b) shear stresses within the core region, and c) principal stresses within the face sheet of the leading edge.

Quantitatively, there is a negligible difference between the extrapolated von Mises stresses at the root section of the heavily loaded spar-box component using the DLOAD subroutine and mapped field methods. This similarity between these methods is valid for stresses in the leading edge component as well. However, notable deviations are observed when compared with the lifting-line methods. The relative difference between method *a* and *b*, Δ_{ab} (in %), is calculated as the absolute value of the difference between the results of method a and method b, divided by the results of method b, and multiplied by 100. The maximum differences between the panel-based and lifting-line methods observed for the von Mises stresses in the heavily loaded spar-box component, for the principal stresses in the face sheet ($\Delta\sigma_{\mathrm{p,facesheet}}$), and for the shear stresses in the core region ($\Delta\tau_{\mathrm{core}}$) of the leading edge component are 12%, 108% and 83%, respectively. A detailed comparison is presented in Fig. 11.

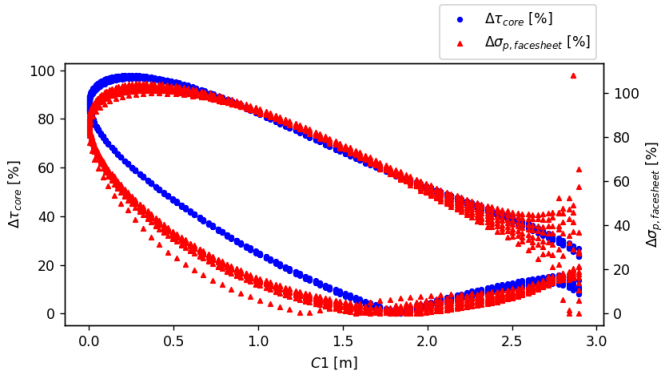

Figure 11. Relative differences in stresses in the leading edge component between panel-based and Lifting-line methods.

Downloaded from http://onepetro.org/JST/article-pdf/11/01/95/5341453/sname-jst-2026-05.pdf/1 by guest on 26 March 2026

The comparative analysis indicates critical implications for structural design and reliability assessment. The prediction of lower local stresses in the leading-edge region by the lifting-line method, while simultaneously predicting higher spar-box stresses. This discrepancy is particularly consequential for sandwich composite structures susceptible to localized failure modes such as core shear failure, face sheet wrinkling, and delamination. The lifting-line method bypasses detailed stress gradients in the chordwise direction, which is a region experiencing the highest aerodynamic pressures during operation. Design decisions based solely on this method may result in under-designed leading-edge structures vulnerable to premature failure.

While mapped field loading and DLOAD subroutine methods demonstrate a realistic representation of distributed aerodynamic load, practical applications must balance computational fidelity with efficiency. A hierarchical modeling strategy is recommended: employing simplified methods for initial sizing and global load estimation, followed by high-fidelity techniques for detailed stress analysis of critical components. The choice of load transfer method should be informed by specific failure modes of concern; the lifting-line method may suffice for main load-bearing spar-box component assessment, whereas local failure modes in sandwich composites necessitate the spatial resolution afforded by mapped loading methods. The deviation in stress results in the leading-edge sandwich composite component, highlighting the importance of accurately modeling the local distribution of aerodynamic loads, especially for a system-level reliability analysis of the wingsail that accounts for the failure probability contributions of individual components.

The single-element wingsail assessment demonstrates that the aeroelastic responses obtained using the DLOAD subroutine and mapped field methods are highly similar, as shown in Figs. 10a–c. This motivates further assessment of the alignment of results of these methods in regions where the maximum discrepancy in aeroelastic response is expected, i.e., the displacement at the top edge of the two-element wingsail. Fig. 12b shows the resultant displacement (ΔD) of nodal points at the top edge of the wings across the chord length of the two-element wingsail. The results imply that the agreement between predictions from the DLOAD and mapped field methods observed in the single-element wingsail also extends to the two-element configuration. The maximum difference of resultant displacement between these two methods at the trailing edge of the flap wing is 2.5 mm.

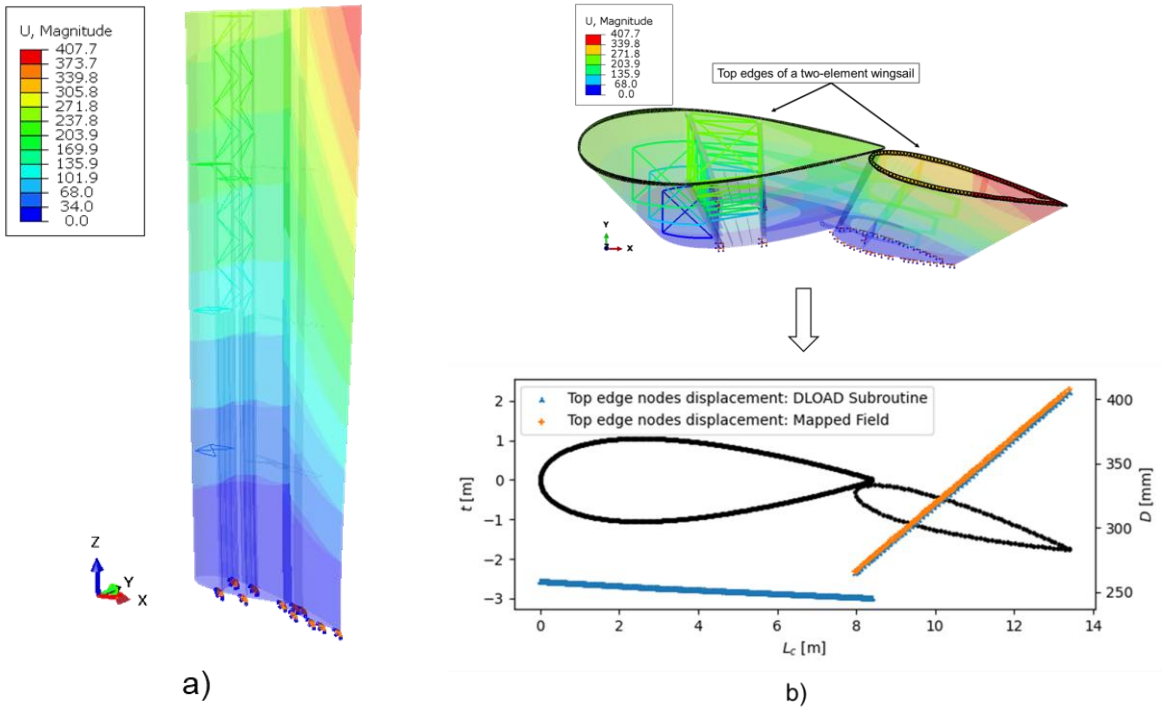

Figure 12. a).The resultant displacement of the global model of Oceanbird's two-element wingsail, and b) resultant displacement of nodal points at the top edges of the two-element wingsail.

Downloaded from http://onepetro.org/JST/article-pdf/11/01/95/5341453/sname-jst-2026-05.pdf/1 by guest on 26 March 2026

The CPU time and wall-clock time in seconds for different core counts are compared across all methods, as shown in Fig. 13. The computational expense of the lifting-line method is lower compared to the panel-based methods. The average CPU time and wall-clock time ratios between the DLOAD subroutine and mapped field methods are approximately 37% and 70%, respectively. This indicates that the DLOAD subroutine method is significantly faster in terms of computational time. Additionally, the CPU time for the mapped field method remains relatively consistent across different numbers of cores, suggesting that data synchronization overhead is minimal as core count increases. This makes the DLOAD subroutine method well-suited for efficient parallelization for Abaqus jobs.

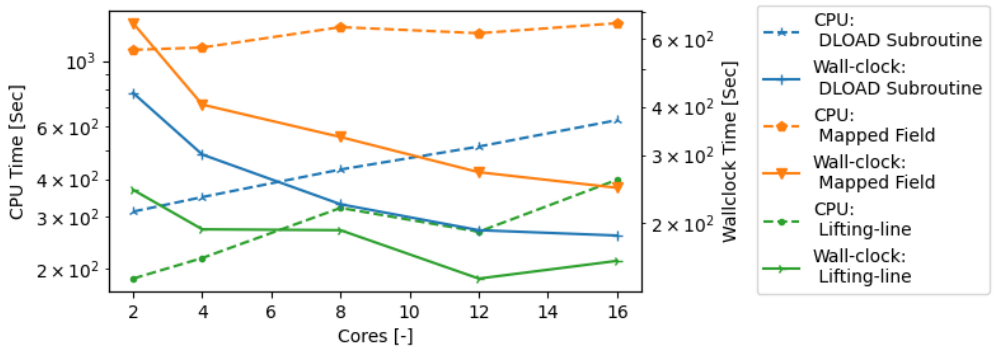

Figure 13. Comparisons of CPU time and wall-clock time.

4. CONCLUSIONS

This study investigated the aeroelastic response of wingsail components using three aerodynamic load transfer techniques: the lifting-line method, panel-based load transfer implemented via a DLOAD subroutine and mapped-field load transfer methods. Each method was evaluated in terms of predicted structural response characteristics and computational time required. Among these three methods, the lifting-line method is computationally the fastest but predicts the highest stresses in the root region of the main load-bearing component compared to the panel-based methods. However, it predicts lower local stresses in the core and face sheet regions at the front tip (nose) of the leading-edge sandwich component. Comparative analysis showed that the DLOAD subroutine and mapped field methods produce highly consistent structural responses across both single-element and two-element wingsail configurations. These methods more effectively capture local variations in aerodynamic loading, which is essential for evaluating stresses in complex, spatially distributed components. From a computational perspective, the DLOAD subroutine method offers a favourable balance between computational fidelity and efficiency, demanding significantly less computational time than the mapped field method while delivering nearly equivalent results. The DLOAD subroutine method demonstrates superior parallel scaling efficiency, with wall-clock time reductions of approximately 30% compared to the mapped field method at higher core counts. The selection of an appropriate load transfer method should be guided by the specific analysis objectives: the lifting-line method may be adequate for preliminary design of the main spar-box component, whereas the panel-based methods (particularly the DLOAD subroutine method) are recommended for detailed stress analysis of sandwich composite components where local failure modes govern structural integrity.

ACKNOWLEDGEMENTS

This work received funds from the European Union's Horizon Europe Research and Innovation program under grant no 101096673. The authors acknowledge Oceanbird for providing the technical drawings and aerodynamic test data of Oceanbird's wingsail design.

Downloaded from http://onepetro.org/JST/article-pdf/11/01/95/5341453/sname-jst-2026-05.pdf/1 by guest on 26 March 2026

REFERENCES

Abdullah, M.S., Ishak, M.H.H. and Ismail, F.(2022). Numerical Study of the 3D Savonius Turbine under Stationary Conditions. *Engineering Failure Analysis* 136. ISSN:13506307. DOI:10.1016/j.engfailanal.2022.106199

Beom Lee, K., Yeon Cho, J. and Ho Kim, J.(2023). Force/Moment-Conserving Pressure Mapping Scheme for Fluid/Structure Interaction Analysis. *AIAA Journal* 61(4), pp. 1462–1474. ISSN:0001-1452. DOI:10.2514/1.j062519.

Boudounit, H., Tarfaoui, M., Saifaoui, D. and Nachtane, M.(2020). Structural Analysis of Offshore Wind Turbine Blades using Finite Element Method. *Wind Engineering* 44(2), pp. 168–180. DOI:10.1177/0309524x19849830.

Buhmann, M., De Marchi, S. and Perracchione, E.(2020). Analysis of a New Class of Rational RBF Expansions. *IMA Journal of Numerical Analysis* 40, pp. 1972–1993. DOI:10.1093/imanum/drz015.

Chiappa, A., Lopez, A. and Groth, C.(2024). Advanced RBF Methods for Mapping Aerodynamic Loads onto Structures in High-Fidelity FSI Simulations. *Fluids* 9(6). ISSN:2311-5521. DOI:10.3390/fluids9060137

Cirello, A., Gulizzi, V., Mancuso, A. and Mirulla, A.I.(2025). Vortex Lattice Method approach to sailing yacht foil design: feasibility and comparison with RANS method results. *International Journal on Interactive Design and Manufacturing* [Preprint]. DOI:10.1007/s12008-025-02378-4.

Deng, Z., Xiao, Q., Huang, Y., Yang, L. and Liu, Y.(2024). A General FSI Framework for an Effective Stress Analysis on Composite Wind Turbine Blades. *Ocean Engineering* 291, p. 116412. ISSN:0029-8018. DOI:10.1016/j.oceaneng.2023.116412.

DNV.(2022).*Wind assisted propulsion systems.* October 20. DNV-ST-0511.

Drela, M.(1989). *XFOIL: An Analysis and Design System for Low Reynolds Number Airfoils BT - Low Reynolds Number Aerodynamics*. Berlin, Heidelberg: Springer pp. 1–12. DOI:10.1007/978-3-642-84010-4_1.

Du, Z., Du, P. and Ning, F.(2024).Coupled Fluid-structure Aeroelastic Analysis of Turbomachinery Using Conservative Data Transfer Algorithm. DOI:10.33737/gpps24-tc-055.

El, Y., Yassen, S., Abdelhameed, A.S. and Elshorbagy, K.A.(2023). An Examination of Hub Wind Turbine utilizing Fluid-Structure Interaction Strategy. *Alexandria Engineering Journal* 64, pp. 1–11. ISSN:1110-0168. DOI:10.1016/j.aej.2022.08.042.

European Commission.(2023).*Wind as Main Propulsion by ORCELLE*. DOI:10.3030/101096673.

Fritz, E.K., Ferreira, C. and Boorsma, K.(2022). An Efficient Blade Sweep Correction Model for Blade Element Momentum Theory. *Wind Energy* 25(12), pp. 1977–1994. ISSN:10991824. DOI:10.1002/we.2778.

Gulizzi, V. and Benedetti, I.(2024). Computational Aeroelastic Analysis of Wings Based on the Structural Discontinuous Galerkin And Aerodynamic Vortex Lattice Methods. *Aerospace Science and Technology* 144, p. 108808. ISSN:12709638. DOI:10.1016/j.ast.2023.108808.

Downloaded from http://onepetro.org/JST/article-pdf/11/01/95/5341453/sname-jst-2026-05.pdf/1 by guest on 26 March 2026

Hillenbrand, A., Giovannetti, L.M., Dhomé, U. and Kuttenkeuler, J.(2024). Wind Tunnel Tests of a Two-Element Wingsail with Focus on Near-Stall Aerodynamics. *Journal of Sailing Technology* 9(01), pp. 110–127. ISSN:2475-370X. DOI:10.5957/jst/2024.9.1.110.

Huque, Z., Zemmouri, F., Lu, H. and Kommalapati, R.R.(2024). Fluid–Structure Interaction Simulations of Wind Turbine Blades with Pointed Tips. *Energies* 17(5). ISSN:1996-1073. DOI:10.3390/en17051090.VON

Von Klemperer, C.J., Horwitz, R.A.D. and Malan, A.G.(2023). An Articulating Wingsail Design for Wind Assisted Ship Propulsion (WASP) Applications. *Scientific African* 20, p. e01699. ISSN:24682276. DOI:10.1016/j.sciaf.2023.e01699.

Ko, A.P.(2022).*Optimization of a Multi-Element Airfoil for a Rigid Airborne Wind Energy Kites*. Delft University of Technology. URL: https://resolver.tudelft.nl/uuid:70cdd6a3-35fa-4008-b52e-8df8f4aaabfa.

Kramer, J.V. and Steen, S.(2022). Sail-Induced Resistance on a Wind-Powered Cargo Ship. *Ocean Engineering* 261(August), p. 111688. DOI:10.1016/j.oceaneng.2022.111688.

Li, C., Wang, H. and Sun, P.(2020). Numerical Investigation of a Two-Element Wingsail for Ship Auxiliary Propulsion. *Journal of Marine Science and Engineering* 8(5). ISSN:2077-1312. DOI:10.3390/jmse8050333 URL: https://www.mdpi.com/2077-1312/8/5/333.

Li, C., Wang, H. and Sun, P.(2023). Study on the Influence of Gradient Wind on the Aerodynamic Characteristics of a Two-Element Wingsail for Ship-Assisted Propulsion. *Journal of Marine Science and Engineering* 11(1). ISSN:20771312. DOI:10.3390/jmse11010134.

Löhner, R.(1995). Robust, Vectorized Search Algorithms for Interpolation on Unstructured Grids. *Journal of Computational Physics* 118(2), pp. 380–387. ISSN:0021-9991. DOI: https://doi.org/10.1006/jcph.1995.1107.

Ma, M., Yao, W., Jiang, W., Jin, W., Chen, Y. and Li, P.(2021). A Multi-Area Fatigue Damage Model of Composite Honeycomb Sandwich Panels Under Three-Point Bending Load. *Composite Structures* 261, p. 113603. ISSN:0263-8223. DOI:https://doi.org/10.1016/j.compstruct.2021.113603.

Reid, J.T. and Hunsaker, D.F.(2021). General Approach to Lifting-Line Theory, Applied to Wings With Sweep. Journal of Aircraft 58(2), pp. 334–346. ISSN:15333868. DOI:10.2514/1.c035994.

Sayed, M., Lutz, T., Krämer, E., Shayegan, S. and Wüchner, R.(2019). Aeroelastic Analysis of 10 MW Wind Turbine using CFD – CSD Explicit FSI-Coupling Approach. *Journal of Fluids and Structures* 87, pp. 354–377. ISSN:0889-9746. DOI:10.1016/j.jfluidstructs.2019.03.023.

Schwab, R.K. and Reid, H.E.(2020). Reduced-Order Modeling and Experimental Studies of Bilaterally Coupled Fluid – Structure Interaction in Single- Degree-of-Freedom Flapping Wings. *Journal of Vibration and Acoustics* 142, pp. 1–8. DOI:10.1115/1.4045920.

Sharma, N., Gibson, R.F. and Ayorinde, E.O.(2006). Fatigue of Foam and Honeycomb Core Composite Sandwich Structures: A Tutorial. *Journal of Sandwich Structures and Materials* 8(4), pp. 263–319. ISSN:10996362. DOI:10.1177/1099636206063337.

Smith, M., Cesnik, C. and Hodges, D.(2000). Evaluation of Some Data Transfer Algorithms for Noncontiguous Meshes. *Journal of Aerospace Engineering* 13. DOI:10.1061/(asce)0893-1321(2000)13:2(52).

Downloaded from http://onepetro.org/JST/article-pdf/11/01/95/5341453/sname-jst-2026-05.pdf/1 by guest on 26 March 2026

Sugar-Gabor, O.(2018). A General Numerical Unsteady Non-Linear Lifting Line Model for Engineering Aerodynamics Studies. *The Aeronautical Journal* 122(1254), pp. 1199–1228. DOI:10.1017/aer.2018.57.

Suzuki, T. and Mahfuz, H.(2018). Fatigue Characterization of GFRP and Composite Sandwich Panels Under Random Ocean Current Loadings. *International Journal of Fatigue* 111, pp. 124–133. ISSN:01421123. DOI:10.1016/j.ijfatigue.2018.02.004.

Valášek, J. and Sváček, P.(2021). *Finite Element Approximations of Fluid-Structure Interaction Problems: Numerical Analysis of Three Approaches of Aerodynamic Forces Evaluation.in Topical Problems of Fluid Mechanics.* Czech Technical University in Prague - Central Library pp. 140–148. DOI:10.14311/tpfm.2021.019.

Vinje Kramer, J. and Steen, S.(2022). Sail-Induced Resistance on a Wind-Powered Cargo Ship. *Ocean Engineering* 261, p. 111688. ISSN:00298018. DOI:10.1016/j.oceaneng.2022.111688.

Xie, H., Shen, C., Fang, H., Han, J. and Cai, W.(2022). Flexural Property Evaluation of Web Reinforced GFRP-PET Foam Sandwich Panel : Experimental Study and Numerical Simulation. *Composites Part B* 234, p. 109725. ISSN:1359-8368. DOI:10.1016/j.compositesb.2022.109725.

Xu, Y.Q. and Peet, Y.(2017). Accuracy And Performance of Fluid-Structure Interaction Algorithms with Explicit Versus Implicit Formulations of the Fluid Solver. *23rd AIAA Computational Fluid Dynamics Conference*, 2017 pp. 1–11. DOI:10.2514/6.2017-3449.

Zenkert, D. and Burman, M.(2011). Failure Mode Shifts During Constant Amplitude Fatigue Loading of GFRP/Foam Core Sandwich Beams. *International Journal of Fatigue* 33(2), pp. 217–222. ISSN:01421123. DOI:10.1016/j.ijfatigue.2010.08.005.

Zhang, Y., Song, Y., Shen, C. and Chen, N.Z.(2023). Aerodynamic and Structural Analysis for Blades of A 15MW Floating Offshore Wind Turbine. *Ocean Engineering* 287(P1), p. 115785. ISSN:00298018. DOI:10.1016/j.oceaneng.2023.115785.

Zhu, H.(2024). *Analysis and Evaluation of Wingsails with Crescent-Shaped Profiles – from Aerodynamics to Aeroelasticity.* Chalmers University of Technology.

Zhu, H., Chernoray, V., Ringsberg, J.W., Yao, H.-D. and Ramne, B.(2024). Fluid-Structure Interaction Analysis of Crescent-Shaped Wingsails. *43rd International Conference on Ocean, Offshore and Arctic Engineering* (OMAE 2024). DOI:10.1115/omae2024-125739.

Downloaded from http://onepetro.org/JST/article-pdf/11/01/95/5341453/sname-jst-2026-05.pdf/1 by guest on 26 March 2026